Ultrasmall Functional Ferromagnetic Nanostructures Grown by Focused Electron-Beam-Induced Deposition

Luis Serrano-Ramón,[†,‡,#] Rosa Córdoba,[‡,§,#] Luis Alfredo Rodríguez,[‡,§] César Magén,[‡,§,⊥,¶] Etienne Snoeck,[∥,¶] Christophe Gatel,[∥,¶] Inés Serrano,[†,‡] Manuel Ricardo Ibarra,[‡,§,¶] and José María De Teresa[†,‡,§,*]

[†]Instituto de Ciencia de Materiales de Aragón (ICMA), Universidad de Zaragoza-CSIC, 50009 Zaragoza, Spain, [‡]Departamento de Física de la Materia Condensada, Universidad de Zaragoza, 50009 Zaragoza, Spain, [§]Laboratorio de Microscopias Avanzadas (LMA), Instituto de Nanociencia de Aragón (INA), Universidad de Zaragoza, 50018 Zaragoza, Spain, [⊥]Fundación ARAID, 50004 Zaragoza, Spain, [∥]CEMES-CNRS 29, rue Jeanne Marvig B.P. 94347 F-31055 Toulouse Cedex, France, and [¶]Transpyrenean Associated Laboratory for Electron Microscopy (TALEM), CEMES-INA, CNRS, Universidad de Zaragoza. [#]These authors contributed equally to this work.

ABSTRACT We have successfully grown ultrasmall cobalt nanostructures (lateral size below 30 nm) by optimization of the growth conditions using focused electron-beam-induced deposition techniques. This direct-write nanolithography technique is thus shown to produce unprecedented resolution in the growth of magnetic nanostructures. The challenging magnetic characterization of such small structures is here carried out by means of electron holography techniques. Apart from growing ultranarrow nanowires, very small Hall sensors have been created and their large response has been unveiled.

KEYWORDS: magnetic nanostructures · focused electron-beam-induced deposition · electron holography · Hall sensors · nanowires

Ferromagnetic nanostructures are currently at the core of many applications in nanotechnology, such as those related to magnetic information storage and sensing,[1] whereas new applications such as magnetic logic[2] and biosensing[3] are being intensively studied. Thus, with the increasing need for size reduction and integration, the growth of ultrasmall ferromagnetic nanostructures and their precise characterization is perceived as one of the bottlenecks to push forward these technologies.

Focused electron-beam-induced deposition (FEBID) techniques rely on the use of a focused beam of electrons, normally provided by a scanning electron microscope (SEM), dissociating a precursor gas to create a local nanodeposit.[4−7] Several advantages of FEBID compared to other growth techniques can be cited: growth on any substrate and at the targeted place thanks to the SEM, arbitrary shape of the deposit, immediate check of the deposit success with the SEM, high lateral resolution, *etc*.

The main issue concerning the applicability of FEBID compared to other nanolithography techniques is the nanodeposit composition. If the precursor molecules are not completely dissociated by the electron beam, unwanted residual elements will be present, jeopardizing the functionality of the nanodeposit. It is usual to produce metallic deposits with the targeted element being less than 50%.[4−7] In the case of magnetic nanodeposits, the content of the magnetic element is of utmost importance as the magnetic properties can quickly degrade with the presence of residues. The situation is fortunate when using $Co_2(CO)_8$ gas precursor and high beam currents because heating effects can assist the molecule dissociation process[8,9] and produce nearly pure cobalt nanodeposits, as some of us have previously shown.[10]

However, the use of high electron beam currents is counter-productive for the high lateral resolution of the nanodeposits, which is the main drawback for the use of this technique in the growth of small-size magnetic-based devices. Previous work could only demonstrate functional cobalt nanostructures with lateral size down to 150 nm.[11] The ultimate resolution of the FEBID technique is extremely high as shown by van Kouwen *et al.* in ref 12, where 3 nm Pt-based dots were grown. Thus, novel approaches to attain the ultimate resolution of the FEBID technique in the case of magnetic materials, different from the use of high beam currents, are needed.

In the present article, we use a Schottky field-emission electron gun with optimized deposition parameters in order to grow cobalt nanostructures by FEBID with unprecedented lateral resolution and nearly pure cobalt content. For example, cobalt nanowires with lateral size below 30 nm can be grown. These nanowires could find applications in information storage, sensing, and

* Address correspondence to deteresa@unizar.es.

Received for review April 18, 2011 and accepted September 21, 2011.

Published online September 21, 2011
10.1021/nn201517r

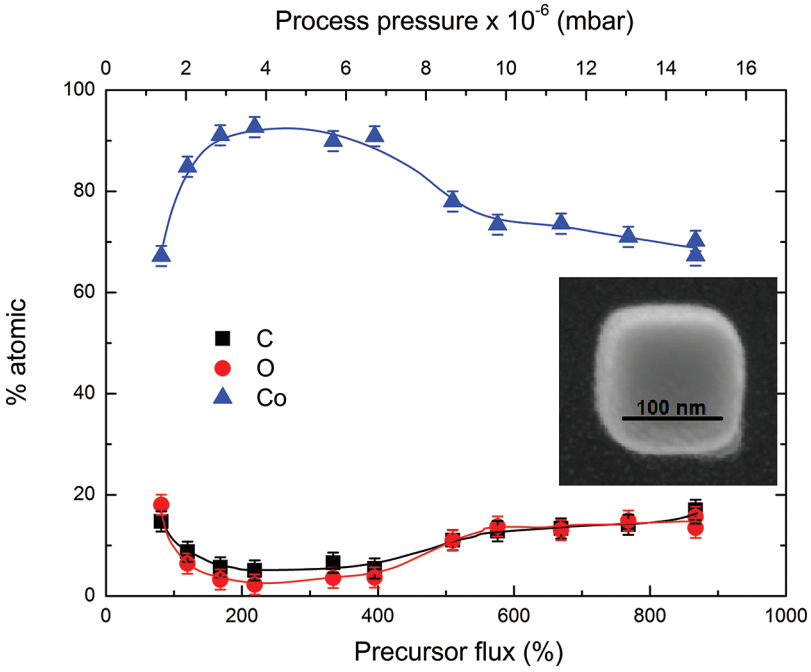

Figure 1. Co atomic percentage in the nanodeposits as a function of the $Co_2(CO)_8$ precursor flux, also monitored by means of the chamber vacuum pressure. Growth was performed with 3 kV electron beam energy and 21 pA current. An SEM image of the typical cobalt squares grown is shown in the inset. The relative change of precursor flux is here defined by the expression: Precursor flux (%) = 100 × ($P_{process}$ − P_{base})/P_{base}.

logic, but their magnetic characterization is challenging, requiring advanced techniques such as electron holography used here. One application of these nanodeposits is shown by growing cobalt nano-Hall probes with an active area close to 100 × 100 nm^2 and sensitivity in the range of 0.1 Ω/T.

RESULTS AND DISCUSSION

First, we describe the experiments performed to achieve the optimized growth of cobalt nanostructures with low beam current. Previous results with the same precursor used by us, $Co_2(CO)_8$, indicate that certain tuning of the Co content can be achieved by finding appropriate growth parameters.[13] Following this approach, we fix a low beam current (in the pA range) as desired to obtain narrow structures and study the influence of the precursor gas flux. In fact, it has been reported that the diameter of the electron beam increases proportionally to the square root of the beam current, thus being a limiting factor for the lateral resolution.[14] In the experiment, cobalt squares with dimensions of 100 nm in lateral size and 100 nm in thickness were grown on silicon. The base pressure in the growth chamber is 1.3 × 10^{-6} mbar, and when the precursor valve is completely open, the pressure rises to 1.8 × 10^{-5} mbar. By gradually opening the gas valve, the precursor flux can be tailored and the chamber pressure will change accordingly and will be monitored. The cobalt nanosquares were grown at a beam energy of 3 kV and beam current of 21 pA. As readily noticed in Figure 1, a clear trend is observed in the cobalt content as a function of the precursor gas flux. A cobalt content around 65%[10] is obtained with the lowest and the highest precursor flux used. However, at intermediate precursor flux values, the cobalt content can be optimized up to 93%. These results can be understood in the following way. At low precursor flux, where the growth is performed within the precursor-limited regime, dissociation of residual species present in the process chamber will play a role producing sample contamination.[13] At high precursor flux, where the growth is performed within the electron-limited regime, the precursor molecules are refreshed too quickly for the electron beam to decompose completely all of the precursor material, which will become incorporated in the nanodeposit. At intermediate precursor flux, where the growth is performed between both regimes, it is possible to reach a perfect balance between the precursor flux, the electron beam current, and the time that the electron beam stays in each point (coined "dwell time", t_{dwell}, 1 μs in the present case). It is thus possible to produce the total decomposition of the precursor material, whereas the incorporation of residual species is avoided. In those growth conditions, small Co nanostructures with high purity can be created.

The fabrication of ultrasmall structures with high Co content requires a fine-tuning of the different parameters, the dwell time becoming relevant too, as shown herafter. We performed experiments where the precursor flux is kept constant at 5.6 × 10^{-6} mbar, the total electron dose per deposit is also kept constant,

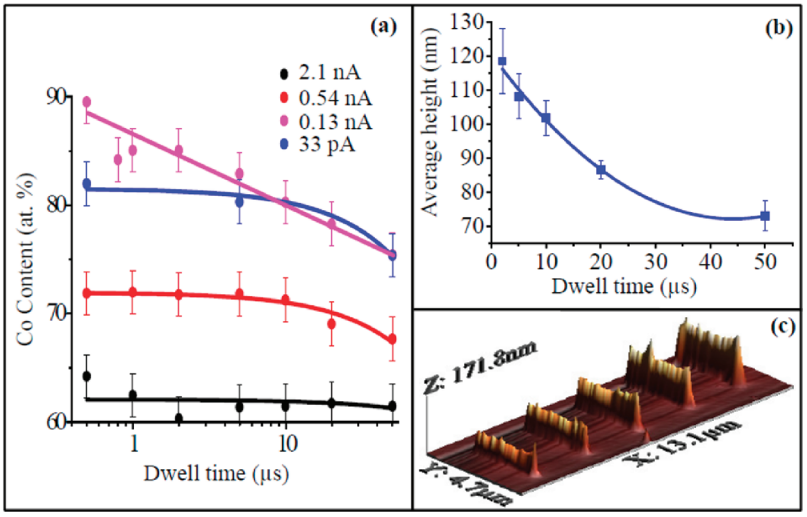

Figure 2. (a) Variation of the Co content of the 600 × 600 nm^2 squares as a function of their dwell time for four different beam currents. The dose and flux were kept constant in all of the samples. The color lines are just a guide for the eye. (b) Average height as a function of the dwell time in Co nanowires grown at 21 pA and 10 kV. The blue line is just a guide for the eye. (c) Three-dimensional plot of the AFM image of the wires used for the study represented in (b).

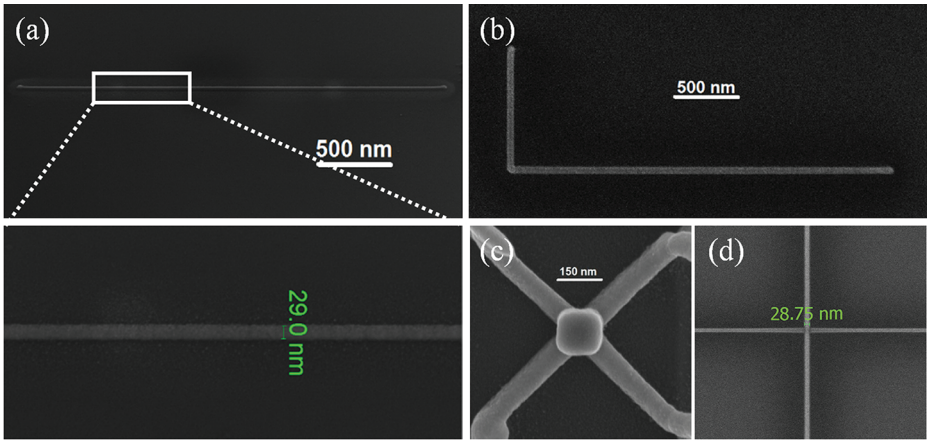

Figure 3. (a) SEM image of a cobalt nanowire with dimensions of 3 μm in length, 29 nm in width, and 30 nm in thickness grown at 3 kV, 21 pA (image taken at tilting angle of 52°). A zoom-in image is shown in the inset (image taken at tilting angle of 0°). (b) SEM image of a cobalt nanostructure (L shape) with dimensions of 3 μm in length for the horizontal part and 1 μm in length for the perpendicular part, 40 nm in width, and 30 nm in thickness, grown at 3 kV, 21 pA (image taken at tilting angle of 0°). (c) SEM image of one cobalt Hall sensor based on four independent 75 nm wide cobalt lines and the central square 150 nm wide active area (image taken at tilting angle of 0°). (d) SEM image of one cobalt Hall cross with a width less than 30 nm (image taken at tilting angle of 0°).

and for different electron beam currents, the dwell time is varied. Squares of size 600 × 600 nm^2 were grown in this experiment, and the obtained Co content is shown in Figure 2a for the different electron beam currents as a function of the dwell time. For 10 kV and 2.1 nA deposition parameters, the Co content is below 65% in all of the studied range of dwell time values, reflecting the lack of full gas replenishment during deposition and the contamination of the deposit with residual chamber molecules. The cobalt content decreases when the dwell time increases because the gas consumption increases at each addressed point. Figure 2a also shows that the metallic content increases significantly when decreasing the beam current as a consequence of the growth in the precursor-limited regime. For all of the studied beam currents, the increase of the dwell time further decreases the metallic content for the same reason. The effect of the dwell time is remarkable when using a beam current of 0.13 nA, for which the Co percent increases from 75 to 90% when the dwell time decreases from 50 μs to 500 ns. The growth parameters for the highest metal content in this case are slightly different from those found in Figure 1 due to the different geometry, which affects the loop time (time spent by the beam to pass again on the same point) and thus the precursor replenishment. These results allow us to conclude that for small Co nanodeposits one has to find the right combination of precursor flux, beam current, and dwell time in order to attain the highest Co content (>90%). Furthermore, the average height of

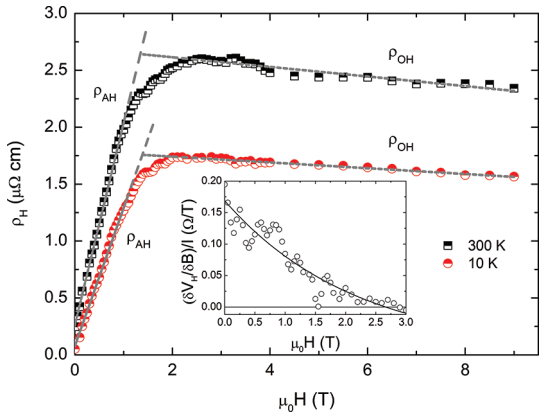

Figure 4. Hall resistivity in the same Co Hall sensor shown in Figure 3c at 300 and 10 K. The inset shows the field sensitivity as a function of the magnetic field at 300 K.

the deposits grown with the same electron dose is strongly influenced by the dwell time as can be noticed in Figure 2b,c, as previously reported for other precursor gases.[15,16] The relevant information inferred from these experiments is that, for low beam currents allowing the growth of narrow structures, it is always possible to find the right combination of dwell time and precursor flux in order to attain cobalt content above 90%.

The quantitative modeling of the growth mechanisms as a function of the above-mentioned relevant parameters due to the existence of the residual background gases along with the precursor molecules is beyond the scope of the present article. However, it can be mentioned that other authors have tackled this important issue[13] and have highlighted the role that could be played by autocatalysis phenomena.[17]

Once the growth conditions for small Co nanodeposits were mastered, we created two types of functional magnetic nanostructures: (1) nano-Hall probes for nanosensing;[18,19] (2) high-purity ultranarrow nanowires with perspectives in applications related to spintronics[20] and magnetic logic based on domain wall manipulation.[21]

Ultrasmall Hall sensors offer the possibility to increase the detection sensitivity down to the order of $10^{-6}\phi_0$ ($\phi_0 = h/2e$ is the flux quantum).[19] The fabrication of such devices at nanometric scale is of outstanding interest in biosensing for the detection of biological moieties conjugated to magnetic nanoparticles and in general for different nanosensing applications (scanning Hall microscopy, nanomagnetometry, proximity switching, current sensing, *etc.*).[22,23] By using FEBID, we have grown Co Hall nanoprobes, as those ones shown in Figure 3c,d.

In Figure 4, the Hall resistivity of the sensor displayed in Figure 3c is represented as a function of the applied magnetic field at 300 and 10 K. The Hall resistivity is given by

$$\rho_H = \frac{V_H t}{I} = \mu_0(R_0 H + R_S M) \qquad (1)$$

where V_H is the measured Hall voltage, t is the cobalt square thickness, and I is the bias current. The ρ_H has contributions from the ordinary (OHE) and anomalous (AHE) Hall effect, where R_0 and R_S are the ordinary and anomalous Hall coefficients, respectively. H is the applied magnetic field, and M is the magnetization. The lines in Figure 4 correspond to the individual contributions from the OHE and the AHE. The crossover from the low-field behavior, positive in sign and dominated by the AHE, to the high-field behavior, negative in sign and dominated by the OHE, takes place around 1.7 T, as occurs in polycrystalline Co thin films[24] and in Co grown by FEBID at high beam current.[10] It is noteworthy that low-Co-content Hall sensors grown by FEBID do not present this clear crossover between the AHE and the OHE.[18,19]

The maximum room-temperature Hall resistivity of the narrow sensors investigated here is around 2.7 $\mu\Omega$cm, 1 order of magnitude higher than that obtained previously in Co nanodeposits grown at high beam current.[10] The difference should be ascribed to the relatively higher longitudinal resistivity of the present cobalt nanodeposits (due to the slightly lower metallic content) as there is a clear correlation between Hall resistivity and longitudinal resistivity.[25] The field sensitivity (S_I) is an important parameter to characterize the Hall sensors (inset of Figure 4c):

$$S_I = \frac{\delta V_H/\delta B}{I} \qquad (2)$$

The low-field S_I of the studied Hall sensors ranges between 0.13 and 0.07 Ω/T. The obtained S_I values are similar to those reported in ref 18 for lower-content Co sensors, but the important figure of merit of nanoscale Hall sensing is the minimum magnetic flux detectable (ϕ_{min}). In ref 19, ϕ_{min} is estimated to be around 2×10^{-6} ϕ_0, which is better than previously reported values in other nano-Hall probes. In the thermal noise regime, ϕ_{min} is proportional to the longitudinal sensor resistance and the sensing area. As both, the longitudinal resistance and the sensing area, are significantly lower in our high-purity narrow Co-based sensors than in ref 19, we expect to improve the figure of merit ϕ_{min} more than 1 order of magnitude. First, we expect an improvement of a factor of 3 due to the smaller sensing area: a factor of 10 smaller area but a decrease of the maximum current attainable in a factor of 3. Second, an improvement of a factor of 10 due to the lower longitudinal resistance can also be expected. Dedicated experiments are required to confirm this issue, which constitutes an exciting future research line in nanoscale sensing.

The second type of functional nanostructures addressed in the present study is represented by narrow nanowires grown using 3 kV beam energy and 21 pA beam current. The corresponding SEM images are displayed in Figure 3a,b, showing an impressive high lateral resolution, around 30 nm, significantly better than previous achievements, where high beam current

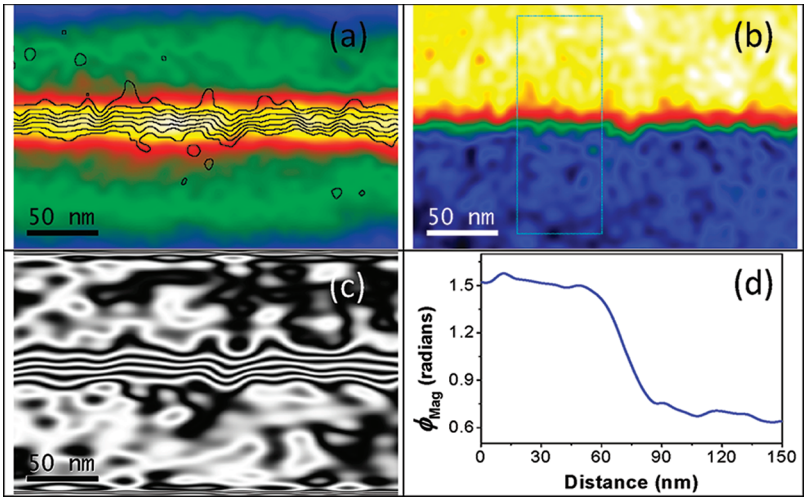

Figure 5. Electrostatic (a) and magnetic (b) contributions to the electron beam phase shift across a Co nanowire with a thickness of 9 nm and a width of 30 nm. The magnetic flux deduced from the "magnetic phase image" is superimposed over the electrostatic phase shift image. (c) Cosine of 38 times the magnetic phase image allowing a better visualization of the magnetic flux within and out of the nanowire. (d) Phase shift profile extracted from the right part of figure (b) where the magnetic induction is constant (see text).

was required to obtain high Co purity.[11] As the magnetic nanostructures become narrower and narrower, they impose stringent conditions for their precise characterization. Fortunately, these Co nanostructures can be directly grown on top of thin Si_3N_4 membranes, allowing their nanoscale quantitative magnetic characterization by means of Lorentz transmission electron microscopy (LTEM) and electron holography (EH) presented hereafter. LTEM and EH were performed on a Titan-Cube microscope fitted with a Cs image corrector and a Lorentz lens. LTEM is a standard TEM tool for studying the magnetic configurations in nanostructures in the range of a few hundred nanometers in size,[26] thus not being accurate enough for quantitative magnetic measurements in small magnets, in particular, for nanostructures smaller than ~50 nm. LTEM analyses have nevertheless been performed on Co deposits (see Supporting Information) for qualitative studies of the magnetic configuration in wider wires. However, quantitative magnetic measurements on such small nanostructures can be achieved by EH.[27−30] To image the remnant magnetic state and get quantitative measurements of the magnetization in even thinner Co deposit, we performed EH on wires of different size. EH allows the amplitude and the phase shift of a high energy electron wave that has passed through a material to be recorded. The phase shift ϕ is sensitive to electric and magnetic fields in the sample[27,28,31] and is given by the expression

$$\phi(x) = C_E \int V(x,z)\mathrm{d}z - \frac{e}{\hbar}\iint B_\perp(x,z)\mathrm{d}x\mathrm{d}z \qquad (3)$$

where x is a direction in the plane of the sample, z is the incident electron beam direction, C_E is a constant dependent on the accelerating voltage of the microscope (6.53×10^6 rad V^{-1} m^{-1} at 300 kV), V is the electrostatic potential of the sample, in our case associated solely to the mean inner potential (MIP) of the wire, and $B_\perp$ is the component of the magnetic induction (both inside the sample and in the surrounding leakage fields) perpendicular to both x and z. To separate the magnetic contribution to the electrostatic one, on each single wire, we took one hologram then switched the sample upside down then took a second hologram. The calculated phase images obtained present the same electrostatic contribution, while the magnetic one is reversed in sign. Image calculations then allow separating the electrostatic contribution ($\phi_{elect.}$) and the magnetic contribution (ϕ_{Mag}) to the phase shift of the electron beam. These two contributions are reported in Figure 5a,b, respectively. The electrostatic contribution $\phi_{elect.} = C_E \times V_{MIP}t$ depends on the thickness and the mean inner potential V_{MIP}, which itself depends on local composition and density. The thicknesses of the different Co nanowires have been measured by AFM, so the MIP can then be determined. It is found to vary from wires to wires between 11 and 17 V. This is slightly lower than what has been measured by De Graef *et al.*[32] (26 V) and to the theoretical values[27] because of the lower density of such nanocrystalline Co wires compared to bulk cobalt.

In Figure 5c, we report the cosines of 38 times the magnetic contribution, which better visualizes the phase gradient corresponding to the magnetic flux. The integration of the magnetic component $\phi_{Mag.}$ along the beam path across the sample permits measuring the magnetic induction $B_\perp$:

$$B_\perp(x) = \frac{\hbar}{et} \times \frac{\partial \phi_{Mag}(x)}{\partial x} \qquad (4)$$

The latter only depends on the physical constant "e" and "$\hbar$", the sample thickness "t", and phase shift across

the field of view. Measuring the phase shift across the wires of different thicknesses then allows calculating the magnetization within these wires.[29] Figure 5d displays the phase shift profile extracted from Figure 5b in an area far from the tip of the wire, so that the magnetic induction is expected to be constant in intensity and direction and concentrated within the Co wire (as checked in Figure 5c). In such 9 nm thick Co wire, the magnetic induction is found to be equal to 1.8 T, which agrees quite well with the bulk magnetization value of cobalt. A second sample with thickness of 37 nm was measured by EH showing reduced magnetization about 20% with respect to the bulk value. Such reduced magnetization could be explained by an overestimation of its thickness in the AFM measurements or a lower cobalt content.

CONCLUSIONS

In conclusion, it has been demonstrated that ultrasmall functional Co magnetic structures with lateral size below 30 nm can be grown by the focused electron-beam-induced deposition technique by fine-tuning of the relevant growth parameters. Their magnetization has been quantitatively characterized by electron holography. This growth technique has been applied to the creation of nano-Hall probes with large potential applications in nanosensing and the creation of ultranarrow nanowires for potential applications in magnetic storage and logic.

EXPERIMENTAL SECTION

For these experiments, we used the $Co_2(CO)_8$ precursor provided by Strem Chemicals Inc., which is stabilized with 1−5% hexane (the CAS number is 10210-68-1). *In situ* compositional analysis of the nanodeposits have been performed by energy-dispersive X-ray microanalysis (EDS) after previous EDS calibration at 3 kV. The samples were inserted in the chamber the day before the deposition is done so that the minimum pumping time is 12 h. The Si_3N_4 membranes do not receive any cleaning treatment in order not to damage them before the deposition and are always stored in the clean room. The Si substrates are cleaned with ultrasound, 3 min in acetone and then 3 more min in isopropyl alcohol.

Additional information on the parameters used during the growth of the different structures is provided hereafter. The current densities in the experiment are the following ones for the beam currents used: 8.1×10^5 A/m^2 (for 0.033 nA), 1.2×10^6 A/m^2 (for 0.13 nA), 1.4×10^6 A/m^2 (for 0.54 nA), 1.5×10^6 A/m^2 (for 2.1 nA).

In the case of the squares reported in Figure 1, the following parameters were used: refresh time = 0, pitch = 4.74 nm, writing strategy = bottom to top scan and multipass. The total dose can be calculated as (current × time)/area = 0.021 nA × 103 s/0.15 μm × 0.15 μm = 96 nC/μm^2. In the case of the squares reported in Figure 2a, refresh time = 0, writing strategy = bottom to top scan, multipass and the total dose is always kept to the value of 100 nC/μm^2.The loop time (time needed to pass again on the same point) for the shorter dwell time (500 ns) is the following one: 15.3 ms/5.6 ms/1.55 ms/0.42 ms, respectively, for the 0.033 nA/0.13 nA/0.54 nA/2.1 nA currents. In order to calculate the loop time for longer dwell time, one just needs to multiply these values by the dwell time divided by 500 ns. In the case of the nanowires reported in Figure 2b,c, there is no refresh time and the total dose is 118 nC/μm^2. The Co/C/O composition of the wires is 83:15:2, 85:11:4, 87:11:2, 84:10:6, and 85:10:5, respectively, for the dwell time values of 2, 5, 10, 20, and 50 μs. The number of passes is 2790, 1117, 559, 280, and 112, respectively, for the dwell time values of 2, 5, 10, 20, and 50 μs. In the case of the 29 nm line shown in Figure 3a, the loop time is 635 μs and the total dose is 118 nC/μm^2. The pattern for the deposition of the L-shaped wires shown in Figure 3b consisted of two single pixel lines deposited in parallel. The direction of deposition was right to left in the horizontal wire and bottom to top in the vertical one. The refresh time was set to 0, and the pitch was 4.74 nm. In the structures grown in Figure 3, the composition (in atomic percentage) measured by EDS after growth of the 150 nm squares is Co/C/O = 93:5:2, whereas in the case of the 30 nm lines, it is 90:8:2. The composition of the Hall sensors shown in the article is Co/C/O = 88:8:4 for the sample with S_I = 0.13 Ω/T and Co/C/O = 84:9:7 for the sample with S_I = 0.07 Ω/T.

The FEBID process depends on aspects which can vary with the substrate such as the rate of secondary electrons reaching the surface layer, the precursor sticking coefficients, the substrate roughness, the water or contaminant molecule adhesion to the surface, *etc*. In order to investigate this point, we have grown cobalt nanodeposits in the same conditions on three different substrates: Si substrates, Si//SiO_2 (300 nm) substrates and Si_3N_4 (50 nm) membranes. Those conditions are as follows: current of 21 pA, voltage of 3 kV, dwell time of 1 μs, no refresh time, square geometry with dimensions of 100 × 100 × 100 nm^3 grown during 102 s and flux optimized for the maximum Co composition. The EDS results indicate only very slight differences in the deposit composition. Thus, we find that the Co/C/O compositions are 85:6:10, 91:2:7, and 85:7:8, respectively, for the Si substrate, Si//SiO_2 substrate, and Si_3N_4 membrane, which indicates irrelevant influence of the substrate on the cobalt growth in the used growth conditions.

The magnetic field produced by the TEM coils in the shown experiments is less than 3 mT. In the whole TEM experiment, the objective lens is switched off to work in field-free conditions. As the magnetic field in the area of the sample is very small (less than 3 mT) and the shape anisotropy is very high due to the high nanowire aspect ratio (length at least 10 times greater than width and thickness), the nanowire is expected to show a monodomain state with the sample magnetization pointing along the nanowire's axis.

Acknowledgment. This work was supported by the Spanish Ministry of Science (through Project MAT2008-06567-C02, including FEDER funding) and the Aragon Regional Government.

Supporting Information Available: Additional information on the Hall devices and the Lorentz transmission electron microscopy is provided. This material is available free of charge *via* the Internet at http://pubs.acs.org.

REFERENCES AND NOTES

1. Chappert, C.; Fert, A.; Van Dau, F. N. The Emergence of Spin Electronics in Data Storage. *Nat. Mater.* **2007**, *6*, 813–823.
2. Allwood, D. A.; Xiong, G.; Faulkner, C. C.; Atkinson, D.; Petit, D.; Cowburn, R. P. Magnetic Domain-Wall Logic. *Science* **2005**, *309*, 1688–1692.
3. Martins, V. C; Germano, J.; Cardoso, F. A.; Loureiro, J.; Cardoso, S.; Sousa, L.; Piedade, M.; Fonseca, L. P.; Freitas, P. P. Challenges and Trends in the Development of a Magnetoresistive Biochip Portable Platform. *J. Magn. Magn. Mater.* **2010**, *322*, 1655–1663.
4. Utke, I.; Hoffmann, P.; Melngailis, J. Gas-Assisted Focused Electron Beam and Ion Beam Processing and Fabrication. *J. Vac. Sci. Technol., B* **2008**, *26*, 1197–1276.

5. van Dorp, W. F.; Hagen, C. W. A Critical Literature Review of Focused Electron Beam Induced Deposition. *J. Appl. Phys.* **2008**, *104*, 081301–081342.
6. Randolph, S. J.; Fowlkes, J. D.; Rack, P. D. Focused Nanoscale Electron-Beam-Induced Deposition and Etching. *Crit. Rev. Solid State Mater. Sci.* **2006**, *31*, 55–89.
7. Botman, A.; Mulders, J. J. L.; Hagen, C. W. Creating Pure Nanostructures from Electron-Beam-Induced-Deposition Using Purification Techniques: A Technology Perspective. *Nanotechnology* **2009**, *20*, 372001.
8. Utke, I.; Michler, J.; Gasser, P.; Santschi, P.; Laub, D.; Cantoni, M.; Buffat, P. A.; Jiao, C.; Hoffmann, P. Cross-Section Investigations of Compositions and Sub-structures of Tips Obtained by Focused Electron Beam Induced Deposition. *Adv. Eng. Mater.* **2005**, *7*, 323–331.
9. Lau, Y. M.; Chee, P. C.; Thong, J. T. L.; Ng, V. Properties and Applications of Cobalt-Based Material Produced by Electron-Beam-Induced Deposition. *J. Vac. Sci. Technol., A* **2002**, *20*, 1295–1302.
10. Fernández-Pacheco, A.; De Teresa, J. M.; Córdoba, R.; Ibarra, M. R. Magnetotransport Properties of High-Quality Cobalt Nanowires Grown by Focused-Electron-Beam-Induced Deposition. *J. Phys. D: Appl. Phys.* **2009**, *42*, 055005.
11. Fernández-Pacheco, A.; De Teresa, J. M.; Szkudlarek, A.; Córdoba, R.; Ibarra, M. R.; Petit, D.; O'Brien, L.; Zeng, H. T.; Lewis, E. R.; Read, D. E.; *et al.* Magnetization Reversal in Individual Cobalt Micro- and Nanowires Grown by Focused-Electron-Beam-Induced-Deposition. *Nanotechnology* **2009**, *20*, 475704.
12. van Kouwen, L.; Botman, A.; Hagen, C. W. Focused Electron-Beam-Induced Deposition of 3 nm Dots in a Scanning Electron Microscope. *Nano Lett.* **2009**, *9*, 2149–2152.
13. Bernau, L.; Gabureac, M.; Erni, R.; Utke, I. Tunable Nanosynthesis of Composite Materials by Electron-Impact Reaction. *Angew. Chem., Int. Ed.* **2010**, *122*, 9064–9068.
14. Mølhave, K.; Nørgaard, D.; Rasmussen, A. M.; Carlsson, A.; Appel, C. C.; Brorson, M.; Jacobsen, C. J. H.; Bøggild, P. Solid Gold Nanostructures Fabricated by Electron Beam Deposition. *Nano Lett.* **2003**, *3*, 1499.
15. Beaulieu, D.; Ding, Y.; Wang, Z. L.; Lackey, W. J. Influence of Process Variables on Electron Beam Chemical Vapor Deposition of Platinum. *J. Vac. Sci. Technol., B* **2005**, *23*, 2151–2159.
16. Kohlmann-von Platen, K. T.; Buchmann, L. M.; Petzold, H. C.; Brünger, W. H. Electron-Beam Induced Tungsten Deposition—Growth Rate Enhancement and Applications in Microelectronics. *J. Vac. Sci. Technol., B* **1992**, *10*, 2690.
17. Utke, I.; Goelzhaeuser, A. Small, Minimally Invasive, Direct: Electrons Induce Local Reactions of Adsorbed Functional Molecules on the Nanoscale. *Angew. Chem., Int. Ed.* **2010**, *49*, 9328–9330.
18. Boero, G.; Utke, I.; Bret, T.; Quack, N.; Todorova, M.; Mouaziz, S.; Kejik, P.; Brugger, J.; Popovic, R. S.; Hoffmann, P. Submicrometer Hall Devices Fabricated by Focused Electron-Beam-Induced Deposition. *Appl. Phys. Lett.* **2005**, *86*, 042503.
19. Gabureac, M.; Bernau, L.; Utke, I.; Boero, G. Granular Co-C Nano-Hall Sensors by Focused Electron-Beam-Induced Deposition. *Nanotechnology* **2010**, *21*, 115503.
20. Sangiao, S.; Morellón, L.; Ibarra, M. R.; De Teresa, J. M. Ferromagnet-Superconductor Nanocontacts Grown by Focused Electron/Ion Beam Techniques for Current-in-Plane Andreev Reflection Measurements. *Solid State Commun.* **2011**, *151*, 37–41.
21. Fernández-Pacheco, A.; De Teresa, J. M.; Córdoba, R.; Ibarra, M. R.; Petit, D.; Read, D. E.; O'Brien, L.; Lewis, E. R.; Zeng, H. T.; Cowburn, R. P. Domain-Wall Conduit Behavior in Cobalt Nanowires Grown by Focused-Electron-Beam-Induced-Deposition. *Appl. Phys. Lett.* **2009**, *94*, 192509.
22. Moritz, J.; Rodmacq, B.; Auffret, S.; Dieny, B. Extraordinary Hall Effect in Thin Magnetic Films and Its Potential for Sensors, Memories and Magnetic Logic Applications. *J. Phys. D: Appl. Phys.* **2008**, *41*, 135001.
23. Sandhu, A.; Kurosawa, K.; Dede, M.; Oral, A. 50 nm Hall Sensors for Room Temperature Scanning Hall Probe Microscopy. *Jpn. J. Appl. Phys.* **2004**, *43*, 777–778.
24. Kötzler, J.; Gil, W. Anomalous Hall Resistivity of Cobalt Films: Evidence for the Intrinsic Spin-Orbit Effect. *Phys. Rev. B* **2005**, *72*, 060412.
25. Nagaosa, N.; Sinova, J.; Onoda, S.; MacDonald, A. H.; Ong, N. P. Anomalous Hall Effect. *Rev. Mod. Phys.* **2010**, *82*, 1539–1592.
26. Kirk, K. J.; Chapman, J. N.; Wilkinson, C. D. W. Lorentz Microscopy of Small Magnetic Structures. *J. Appl. Phys.* **1999**, *85*, 5237–5242.
27. Tonomura, A. Electron-Holographic Interference Microscopy. *Adv. Phys.* **1992**, *41*, 59–103.
28. Dunin-Borkowski, R. E.; McCartney, M. R.; Smith, D. J. Electron Holography of Nanostructured Materials. In *Encyclopaedia of Nanoscience and Nanotechnology*; Nalwa, H. S., Ed.; American Scientific Publishers: Stevenson Ranch, California, 2004; Vol. 3, pp 41−100.
29. Snoeck, E.; Dunin-Borkowski, R. E.; Dumestre, F.; Renaud, P.; Amiens, C.; Chaudret, B.; Zurcher, P. Quantitative Magnetization Measurements on Nanometer Ferromagnetic Cobalt Wires Using Electron Holography. *Appl. Phys. Lett.* **2003**, *82*, 88–90.
30. Takeguchi, M.; Shimojo, M.; Furuya, K. Fabrication of Magnetic Nanostructures Using Electron Beam Induced Chemical Vapour Deposition. *Nanotechnology* **2005**, *16*, 1321–1325.
31. Rau, W. D.; Schwander, P.; Baumann, F. H.; Höppner, W.; Ourmazd, A. Two-Dimensional Mapping of the Electrostatic Potential in Transistors by Electron Holography. *Phys. Rev. Lett.* **1999**, *82*, 2614–2617.
32. de Graef, M.; Nuhfer, T.; McCartney, M. R. Phase Contrast of Spherical Magnetic Particles. *J. Microsc.* **1999**, *194*, 84–94.